Journal of Advanced College of Engineering and Management

Performance-Based Finite Element Investigation of Concrete-Filled Steel and FRP Tubular Columns under Axial Compression

[1,2*]Anish Thapa Magar, [1]Sayana Kandel, [1]Suyogya Shrestha, [1]Sneha Shah, [1]Rohini Thakur
[1]Department of Civil Engineering, Advanced College of Engineering and Management,
Tribhuvan University, Kathmandu 44614, Nepal
[2]Department of Civil Engineering, Himalayan Whitehouse College of Engineering and
Management, Purbanchal University, Kathmandu 44600, Nepal
Corresponding email: [1]anishthapamagar2054@gmail.com*

DOI: 10.3126/jacem.v12i01.93948

Abstract

Reinforced concrete columns are prone to brittle failure under larger axial and seismic loads, highlighting the need for improved structural systems. Although concrete-filled steel tube (CFST) and concrete-filled FRP tube (CFFT) columns offer enhanced performance due to confinement effects, limited studies provide a direct comparison within a unified framework. This paper presents a comparative evaluation of CFST and CFFT columns using finite element modelling in Abaqus, based on confined concrete damage plasticity model for infilled concrete, a plasticity model for steel tubes, and the Hashin damage model for FRP tubes, with validation against experimental results available in the literature. A parametric study was conducted by varying tube thickness, rebar diameter, tube cross-sectional shape, and slenderness ratio. The results showed that increasing the tube thickness from 2 mm to 8 mm enhanced the peak strength of CFST and CFFT columns by 69.54% and 55.6%, respectively, while increasing the rebar diameter from no reinforcement to 16 mm improved the peak strength by 45.6% and 58.36%, respectively. Columns with circular sections exhibited superior performance due to uniform confinement, whereas non-circular sections showed reduced strength. Increasing the slenderness ratio reduced load-bearing capacity and flexural stiffness, thereby increasing buckling susceptibility. Overall, CFST columns exhibited higher strength and stiffness, whereas CFFT columns showed greater ductility because the FRP tube provides effective lateral confinement, allowing greater expansion of the concrete core before rupture. However, due to the relatively low elastic modulus of FRP, its contribution to axial stiffness remains limited.

Keywords*—Concrete-filled steel tube (CFST), Concrete-filled FRP tube (CFFT), Finite element modelling, Stiffness, Ductility, Load-bearing capacity*

1. INTRODUCTION

Concrete-Filled Steel Tube (CFST) and Concrete-Filled Fiber-Reinforced Polymer Tube (CFFT) have been utilized widely on modern structures like buildings, bridges, and skyscrapers due to their high structural efficiency compared to normal RCC structures [1]. While these columns are well-suited for seismic regions, their use remains limited in Nepal due to several reasons, such as the requirement for skilled workers, limited knowledge of composite structures, lack of budgets, inadequate research, and technical guidelines. However, a recent initiative by the government of Nepal has allocated a budget for the construction of a single-tube CFST-type arch bridge above the Budhi Gandaki River in Sauraha, with a total span estimated to be 120 m, and a clear span of 80 m [2]. Furthermore, the introduction of CFFT in Nepal is essential, as it provides better resistance to corrosion in harsh environments and areas like heavy rainfall, high humidity, river valleys, and tunnels [3]. This requires proper research in Nepal to develop guidelines, technical standards, and optimal design strategies for CFST and CFFT columns, while evaluating their feasibility, performance, and potential benefits.

Previous studies have focused primarily on individual material properties or specific aspects like tube thickness or rebar diameter, but have rarely offered a comprehensive comparison of CFST and CFFT columns under axial loading conditions [4], [5], [6]. Furthermore, most of these studies fail to integrate multiple influencing parameters, such as tube thickness, rebar diameter, cross-sectional shape, and slenderness ratio [7], [8], [9]. Hao et al. [10] performed a numerical analysis of square CFST columns and found that when the shear strength and deformation capacity of the column were increased, the axial compression decreased. Nevertheless, the study did not include a comparative analysis between the CFST and CFFT columns. Li et al. [11] developed a mechanism-based uniform design approach for CFST columns with various cross-sectional profiles. Their study showed that the corner radius significantly influences the confinement behavior and has a direct relationship with the confining stress. However, their study was limited to cross-sectional parametric analysis and an analytical model. Alnemrawi et al. [12] investigated the behavior of the CFST columns filled with lightweight concrete and found that the ductility of the column can be further enhanced by using lightweight concrete. Although they conducted a study on slenderness ratio, their study only focused on circular sections and did not explore other profiles or propose an improved design formulation. Muhammad et al. [13] investigated the structural performance of cross-shaped CFST columns under concentric and eccentric loading through experimental and numerical analysis. Their results showed that an increase in height-to-width ratio and eccentric loading minimizes the strength of the columns, while the developed FEM model showed good correlation with the experimental results. However, they did not include a comparative analysis with other composite systems, such as CFFT columns, and the study was limited to cross-shaped CFST sections.

On the other hand, studies on CFFT columns have also been conducted with certain limitations. Huang et al. [14] performed the experimental and numerical analysis of steel fiber reinforced CFFT columns under eccentric loading, and found that the angle of fiber winding significantly affects the strength of the columns. Nonetheless, their study focused on the geopolymer concrete-based CFFT columns and did not include a comparison evaluation of the structural mechanisms between CFST and CFFT columns. Khan et al. [15] investigated the axial behavior of CFRP- and GFRP-confined CFFT columns and reported that FRP tube thickness, types of FRP, and confinement ratio significantly impact the behavior of columns. The Lam and Teng model [16] was employed to compare the stress-strain behavior with analytical models. However, the study was limited to the experimental investigations and analytical models, and other parametric studies were not taken into consideration. Abdallah et al. [17] developed an FEM model to investigate the uniaxial behavior of CFFT columns and found that the parameters such as fiber orientation, FRP layers, and reinforcement ratio significantly affect axial behavior. But the influence of the steel tube confined concrete and the cross-sectional area were not considered in their study. Raza et al. [18] performed FEM analysis of FRP reinforced CFFT columns under concentric and eccentric loading in Abaqus software, and developed an empirical model to predict the axial strength, which showed good accuracy. However, the study was limited to FRP-based systems and did not evaluate the ductility and stiffness of the columns.

Although much research has been conducted on CFST and CFFT columns, most of them have focused on individual parameters and have not considered multiple influencing factors together. In addition, only limited research has directly compared the behavior of CFST and CFFT columns within a single framework [19], [20], [21]. To address these gaps, a detailed study is done in this paper using the finite element method in Abaqus software [22]. The key novelty of this work is the combined investigation of both CFST and CFFT columns by considering important parameters such as tube thickness, rebar diameter, cross-sectional shape, and slenderness ratio, and their impact on the structural performance of the columns. These parameters were selected because they directly govern the confinement effect, load-bearing capacity, stiffness, and ductility of composite columns [23], [24]. Furthermore, the developed FEM model showed good agreement with results reported in the literature, indicating its reliability and potential for use in future studies. The findings of this research are expected to improve understanding of composite column behavior and support the development of practical design guidelines, particularly in the context of Nepal, where the use of such systems is still developing.

2. FINITE ELEMENT MODELLING OF CFST AND CFFT COLUMN

A. Modelling Overview

First and foremost, the concrete-filled steel tube (CFST) column and concrete-filled fiber-reinforced polymer tube (CFFT) column, subjected to an axial load, were validated with an existing study, Wu et al. (CFST-2 model) [25], and Mohamed et al. (A60S30 model) [26], respectively, to verify the accuracy of the proposed model using Abaqus software. These models were chosen because they closely match the geometry, material properties, and loading conditions required for this study. In addition, these papers were well recognized in the literature, and all the data necessary required for finite element modelling (FE) were available.

In the Wu et al. [25] CFST-2 model, the circular concrete column of diameter 110 mm and height 350 mm, was confined with a steel tube of thickness 2 mm, while in the Mohamed et al. [26] A60S30 model, the circular concrete column of diameter 152 mm and height 608 mm, was confined with a FRP tube of 2.65 mm. Six reinforcement bars of 11.3 mm diameter with two stirrups near the end of the column were utilized in the CFFT A60S30 model [26], while no reinforcement bars were utilized in the CFST-2 model [25]. The detailed drawing of the CFST column (CFST-2 model) and CFFT column (A60S30 model) is shown in Figure 1.

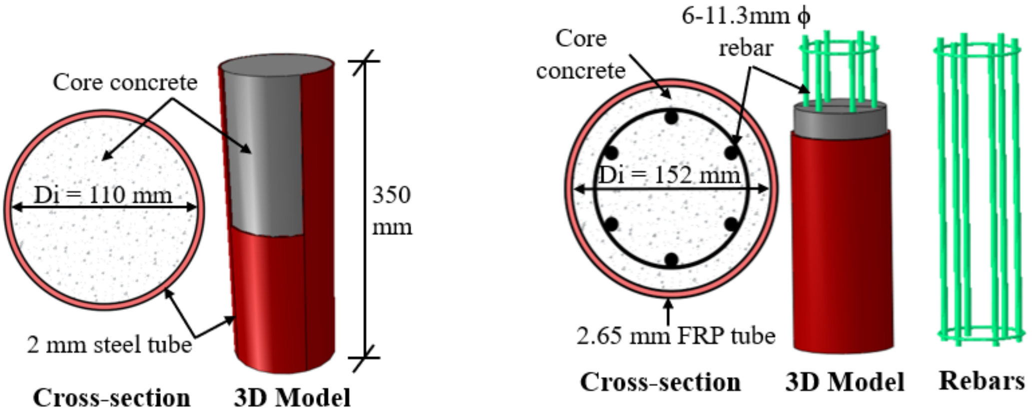

(a) CFST column (CFST-2 model) [25]

(b) CFFT column (A60S30 model) [26]

Figure 1: Detail drawing of validated CFST and CFFT column

B. Material Constitutive Laws

a. Core Concrete in CFST column

The confinement effect should be considered when the concrete, covered or encased by the steel tube, is subjected to an axial load or stresses. In the CFST column, the lateral expansion of the concrete is resisted by the steel tube until the plastic stage in the steel tube begins, so the confinement factor (ξ) is developed, which is shown in Eq. (1) [27], [28].

$$\xi = \frac{A_s f_y}{A_c f_{cc}^{'}} = \alpha \frac{f_y}{f_{cc}^{'}} \tag{1}$$

Where, A_s and f_y represent the cross-sectional area and yield-strength of the steel tube, respectively; A_c and $f_{cc}^{'}$ represent cross-sectional area and cube strength of the core concrete, respectively; α ($=A_s/A_c$) represents the steel ratio.

The constitutive model for compressive behavior of encased concrete in CFST column, which was developed by Han et al. [29], is adopted in this research as shown in Eq. (2) to Eq. (7). This model was utilized in this study because it accounts for the confinement effect provided by the steel tube, which plays a critical role in improving the ductility and compressive strength of the CFST columns. However, this model is developed based on specific experimental conditions and may have limited applicability outside the calibrated range of material properties and confinement levels. For tension behavior of encased concrete, the effect of confinement is very minimal, so the unconfined model proposed by D.J Carreira and K.H Chu [30] is utilized in this research, as shown in Eq. (8) and Eq. (9). This model is adopted in this study because it considers the non-linear tensile response and cracking behavior of concrete, while maintaining computational simplicity.

$$y=\frac{\sigma_c}{\sigma_c'}=\begin{cases}2x-x^2 & x\leq 1\\ \dfrac{x}{\beta_0(x-1)^{\eta}+x} & x>1\end{cases} \tag{2}$$

$$x=\varepsilon/\varepsilon_0 \tag{3}$$

$$\varepsilon_o=\varepsilon_c+800\xi^{0.2}\times 10^{-6} \tag{4}$$

$$\varepsilon_c=(1300+12.5f_{cc}')\times 10^{-6} \tag{5}$$

$$\eta=\begin{cases}2 & x\leq 1\ (Circular\ \ CFST)\\ 1.6+1.5x & x>1\ (Rectangular\ \ CFST)\end{cases} \tag{6}$$

$$\beta_o=\begin{cases}(2.36\times 10^{-5})^{[0.25+(\xi-0.5)^7]}(f_{cc}')^{0.5}\times 0.5\geq 0.12\ (Circular\ \ CFST)\\ \dfrac{(f_{cc}')^{0.1}}{1.2\sqrt{1+\xi}} \qquad (Rectangular\ \ CFST)\end{cases} \tag{7}$$

Where σ_c'(=f_{cc}') is the concrete peak compressive stress corresponding to the strain value, ε_0; σ_c is the confined concrete compressive stress at a certain strain value, ε_c.

$$y_t=\frac{\sigma_t}{\sigma_t'}=\frac{\beta(\varepsilon_t/\varepsilon_t')}{\beta-1+(\varepsilon_t/\varepsilon_t')^{\beta}} \tag{8}$$

$$\beta=\frac{1}{1-\dfrac{f_{cc}'}{\varepsilon_c' E_{ii}}} \tag{9}$$

Where σ_t' is the concrete peak tensile stress corresponding to the strain value, ε_t'; σ_t is the concrete tensile stress at a certain strain value, ε_t; β value depends on the shape of the unconfined compressive stress-strain curve (taken similar to β for unconfined compressive behavior of concrete); E_{ii} is the initial tangent modulus of the compressive stress-strain curve.

The concrete damage plasticity (CDP) model was defined in Abaqus under uniaxial loading for both compression and tension zone, as demonstrated in Figure 2. The damage factor, d, proposed by Mazars et al. [31] was utilized in this study to define the damage of the concrete under compression and tension, which is shown in Eq. (10), while the modulus of elasticity, E_c, was calculated based on [32], as shown in Eq. (11). This damage factor accurately captures the progressive stiffness degradation of the concrete caused by micro-cracking under both tensile and compressive loading.

$$d = 1 - \sqrt{\frac{\sigma}{E_c \varepsilon}} \tag{10}$$

$$E_c = 4700\sqrt{f_{cc}^{'}} \tag{11}$$

The inelastic strain or cracking strain (ε_c^{in} or ε_t^{in}) is required to be input in Abaqus, which was calculated by subtracting the elastic strain ($\varepsilon_{oc}^{el} = \sigma_c/E_c$ or $\varepsilon_{ot}^{el} = \sigma_t/E_c$) from the total strain (ε_{c} or ε_t), as shown in Eq. (12).

$$\begin{aligned} \varepsilon_c^{ck} &= \varepsilon_c - \varepsilon_{oc}^{el}, \text{ for compression} \\ \varepsilon_t^{ck} &= \varepsilon_t - \varepsilon_{ot}^{el}, \text{ for tension} \end{aligned} \tag{12}$$

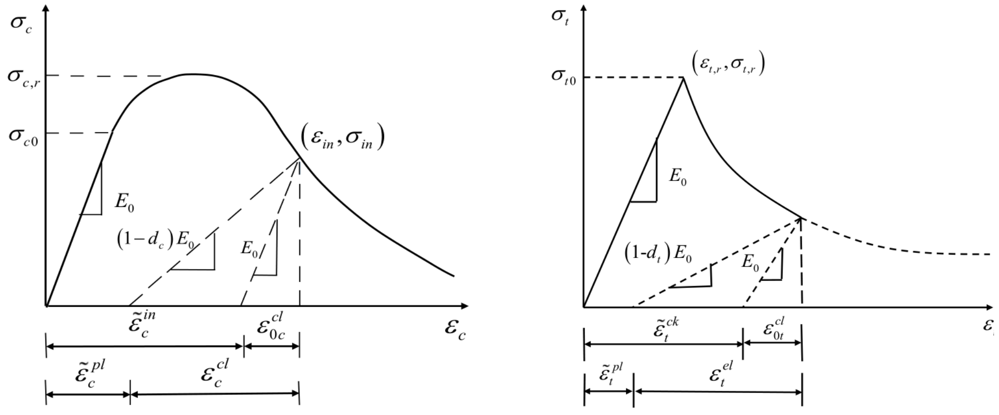

(a) Compression (b) Tension

Figure 2: Response of concrete to uniaxial loading [33]

After defining, the CDP model based on stress-strain curve, the CDP parameters such as dilation angle (ψ), ratio of the second stress invariant on the tensile meridian to that on the compressive meridian (K_c), ratio of equal biaxial to initial compressive yield strength (f_{b0}/f_{c0}), flow potential eccentricity (e), and viscosity parameter (μ) must be defined in Abaqus software to simulate the stress, strain, and failure behavior of concrete. There is no significant effect of flow potential eccentricity (e) and viscosity parameter (μ) in the confined concrete model [34], so the default value presented by Han et al. [29] of 0.1 and 0, respectively, was adopted, as they ensure numerical stability without significantly affecting the accuracy of results. On the other hand, the CDP parameters, such as f_{bo}/f_{c0}, K_c, and ψ, can significantly affect the results [34], [35]. These parameters should be considered while defining the behavior of confined concrete in Abaqus. The f_{bo}/f_{c0} ratio is defined using Eq. (13), which was proposed by Papanikolaou and Kappos [35], because it provides a reliable estimation of the biaxial strength enhancement of concrete.

$$f_{b0} / f_{co} = 1.5\left(f_{cc}^{'}\right)^{-0.075} \tag{13}$$

The ratio of the second stress invariant on the tensile meridian to that on the compressive meridian (K_c) can be determined using Eq. (14), which was proposed by Yu et al. [36] and later modified by Zhong et al. [34], as it offers an improved representation of yield surface shape for confined concrete under multiaxial stress conditions.

$$K_c = \frac{5.5}{5 + 2(f_{cc}^{'})^{0.075}} \tag{14}$$

The dilation angle (ψ) is a function of confinement factor (ξ), so it is directly affected by the confining stress and plastic deformation of the concrete [36]. The dilation angle for different CFST columns is determined based on Eq. (15), which was proposed by Zhong et al. [34]. Furthermore, these equations consider the influence of confinement on the dilation behavior of concrete, making them suitable for our study.

$$\psi = \begin{cases} 56.3(1-\xi) & for\ \xi \leq 0.5 \\ 6.672 e^{\frac{7.4}{4.64+\xi}} & for\ \xi > 0.5 \end{cases} \tag{15}$$

Where the confinement factor (ξ) is determined using Eq. (1).

As explained earlier, CDP parameters are sensitive to input parameters such as dilation angle (ψ), K_c, and f_{b0}/f_{c0} ratio, and also these parameters can affect the behavior of the load-displacement curve. So, the accuracy of the results depends on the appropriate parameter selection and validation against experimental data. In addition, the CDP models do not capture the micro-level cracking mechanisms of the concrete because they assume simplified damage evolution, which is a limitation of this model.

b. Core Concrete in CFFT column

Similar to the CFST column, the concrete encased by FRP Tube also develops a confinement effect, which should be considered while defining the material properties in the FEM model. So, the model proposed by Richart et al. [37] and later developed by Lam and Teng et al. [16] is utilized in this research to define the confined concrete model in Abaqus as shown in Eq. (16) and Eq. (18). This model effectively captures the confinement behavior provided by FRP materials and has been widely utilized in previous studies [17], [38]. However, this model assumes uniform confinement and may not fully capture localized effects or variations in FRP properties under complex loading conditions. According to this model, linear branch of the stress-strain curve is defined as unconfined concrete, while the non-linear branch of the curve is defined by considering the confinement provided by the FRP tube. The stress-strain curve for the FRP-confined concrete model proposed by Lam and Teng et al. [16] is shown in Figure 3.

$$\frac{f_{cc}^{'}}{f_{co}^{'}} = 1 + 3.3\frac{f_{l,a}}{f_{co}^{'}} \tag{16}$$

$$\frac{\varepsilon_{cu}}{\varepsilon_{co}} = 1.75 + 12\left(\frac{f_{l,a}}{f_{co}^{'}}\right)\left(\frac{\varepsilon_{h,rup}}{\varepsilon_{co}}\right)^{0.45} \tag{17}$$

$$f_{l,a} = \frac{2f_f t_f}{D} \tag{18}$$

Where f_{cc}’ is the compressive strength of the confined concrete corresponding to confined strain, ε_{cu}; f_{co}’ is the cylindrical compressive strength of the unconfined concrete corresponding to confined strain, ε_{co} (= 0.0035), which value is taken according to ACI code [32] and Euro code 2 [39]; $f_{l,a}$ is the FRP tube lateral confining pressure; t_f is the FRP tube thickness; f_f is the FRP tube tensile strength; $\varepsilon_{h,rup}$ is the FRP tube hoop strain at rupture point, generally taken as 0.02.

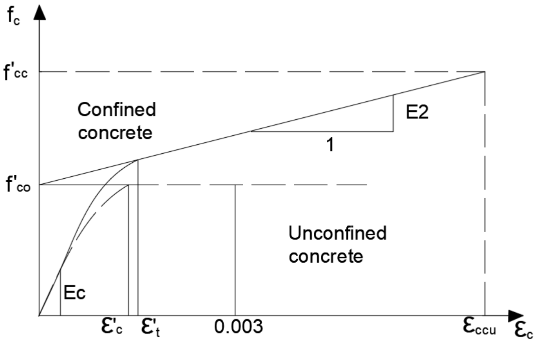

Figure 3: Stress-strain curve FRP confined concrete proposed by Lam and Teng [16]

Eq. (19) shows the transition strain, ε_l, at which the second branch of the stress-strain curve joins the first linear branch. The calculation method for the slope of the second linear branch, E_2, of the stress-strain curve was defined using Eq. (20), while the elastic modulus, E_c, was defined using Eq. (11). The stress at which the second linear branch intersects the stress axis is given by Eq. (21), which was proposed by Samaan et al. [40].

$$\varepsilon_l = \frac{2f_0}{(E_c - E_2)} \tag{19}$$

$$E_2 = \frac{f'_{cc} - f_o}{\varepsilon_{cu}} \tag{20}$$

$$f_o = 0.872 f'_{co} + 0.371 f_l + 6.258 \tag{21}$$

Where, f_0 is the intercept of the stress axis by the linear second portion, and f_l is the equivalent maximum confining pressure.

For the CFFT column, the damage factor and inelastic strain were defined in Abaqus similarly to the CFST column, as shown in Eq. (10) and Eq. (12), respectively. Simultaneously, the CDP parameters for CFFT, such as ratio of tensile strength to compressive strength (f_{b0}/f_{c0}), ratio of the second stress invariant on the tensile meridian to that on the compressive meridian (K_c), and dilation angle (ψ) were defined using Eq. (13), Eq. (14), and Eq. (15), respectively.

In this study, all the CDP parameters, including stress-strain curve, damage parameters, and inelastic strain, were calculated using the above equations and validated against the results available in the literature [25], [26]. For CFST-2 model [25], the elastic modulus (Ec), poisson's ratio (v), and density of the confined concrete were adopted as 29000 MPa, 0.22, and 2400 kg/m3, respectively, while for A60S30 CFFT model [26], these values were adopted as 41620 MPa, 0.3, and 2400 kg/m3, respectively. Similarly, the CDP parameters, including dilation angle (ψ), ratio of the second stress invariant on the tensile meridian to that on the compressive meridian (K_c), ratio of equal biaxial to initial compressive yield strength (f_{b0}/f_{c0}), flow potential eccentricity (e), and viscosity parameter (μ), for CFST-2 model were defined as 28°, 0.717, 1.12, 0.1, and 0, respectively. Similarly, for the A60S30 CFFT model, these values were defined as 36°, 0.707, 1.08, 0.1, and 0, respectively.

1. Steel tube and reinforcement bars

In this study, the bilinear strain-hardening approach is adopted for steel tubes and reinforcement bars, which assumes that the true stress and strain correspond to the nominal stress and strain, while the excessive displacement of the material is neglected. This model is also known as the elastic-plastic model, and is directly available in the Abaqus software [ref]. The stress-strain curve for this constitutive model is shown in Figure 4, while the relationship between them is shown in Eq. (22).

$$\sigma = \begin{cases} E_0\varepsilon & (0 \leq \varepsilon \leq \varepsilon_y) \\ f_y + E_s(\varepsilon - \varepsilon_y) & (\varepsilon_y < \varepsilon) \end{cases} \tag{22}$$

Where E_0 stands for the elastic modulus of steel, E_s stands for strain-hardening stiffness, taken as 0.01 times E_0; f_y stands for yield strength at corresponding strain ε_y, and f_u stands for ultimate strength at corresponding strain ε_u.

The material properties were assigned in Abaqus [22] for the steel tube of the CFST-2 model, which includes a density of 7850 kg/m3, and elastic modulus (E_0) of 196000 MPa, yield strength (f_y) of 381 MPa, and ultimate strength (f_u) of 543 MPa. Similarly, the reinforcement bars were available in the CFFT column (A60S30 model), so these values were adopted as 7850 kg/m3, 209000 MPa, 462 MPa, and 577 MPa, respectively.

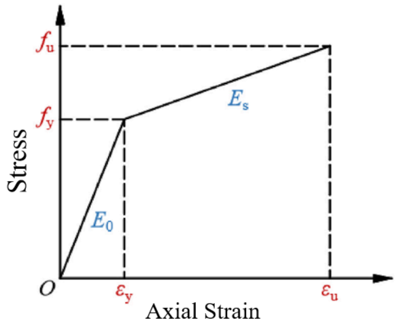

Figure 4: Stress-strain curve for elastic-plastic model

2. **Fiber-reinforced polymer (FRP) tube**

For the FRP tube in the A60S30 model [26], the composite layup module available in Abaqus software [22] was utilized to create ply-count and define discrete layup orientation. The elastic behavior of the FRP tube was modelled utilizing the classical lamina theory, while the damage behavior was modelled using the Hashin damage model. The thickness of each ply-count was adopted as 0.442 mm (total thickness = 2.65 mm), while the rotation angle was adopted as ±60°, as shown in Figure 5. Material stiffness degradation starts when any of the Hashin damage criteria is reached, while the corresponding damage evolves and is governed by the energy-based law with linear softening. This damage evolution continues until the maximum damage is reached, after which no stiffness degradation occurs. Table 1 illustrates the mechanical properties of the FRP tube, while Table 2 illustrates the Hashin-damage parameters of the FRP tube. A detailed mesh-sensitive analysis of FRP tubes was carried out in this study, including the analysis of damage patterns, as discussed in detail in Section 2.4.

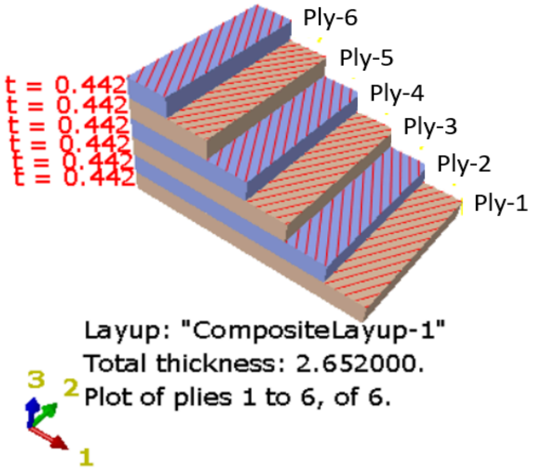

Figure 5: Ply stack plot for FRP tube

Table 1: Mechanical properties of FRP tube [26]

E_1 (MPa)	E_2 (MPa)	v_{12}	G_{12} (MPa)	G_{13} (MPa)	G_{23} (MPa)
20690	8785	0.31	5200	5200	3400

Note: E_1 and E_2 stand for elastic modulus in the fiber direction-1 and direction-2, respectively; v_{12} stands for Poisson's ratio; G_{12}, G_{13}, and G_{23} stand for shear modulus in the 1-2 plane, 1-3 plane, and 2-3 plane, respectively.

Table 2: Hashin damage parameters of FRP tube [26]

Longitudinal tensile strength (MPa)	Longitudinal compressive strength (MPa)	Transverse tensile strength (MPa)	Transverse compressive strength (MPa)	Longitudinal shear strength (MPa)	Transverse tensile strength (MPa)
345	140	40	40	20	20

C. Finite element type, interaction, and boundary condition

For concrete in both the CFST-2 model and A60S30 CFFT model, a 3D continuous solid element (C3D8R) and an 8-node brick element were utilized, while both steel tube and FRP tube were defined using a 4-node linear shell element (S4R). Since rebars were available in the A60S30 CFFT model, they were defined using 2-node linear truss elements (T3D2). A reference point was created at the top of both models (CFST and CFFT), and coupled with the top surface of the model, including concrete and steel or FRP tube. The axial load was applied using a displacement-controlled method (tabular amplitude) in the reference point in the y-axis direction, while the bottom surface of the model was fixed using the ENCASTRE (U1=U2=U3=UR1=UR2=UR3=0) boundary condition to resist the applied load. The surface-to-surface interaction was defined between concrete and steel tube using a tangential behavior with a coefficient of friction of 0.65 [41], [42], and normal contact behavior with hard contact. Similarly, the interaction between the concrete and FRP tube was modeled using tangential behavior with a friction coefficient of 0.25 and hard contact in the normal direction [18]. The impact of bond-slip behavior can be considered through cohesive interaction, but it requires detailed interface properties that are not available in the present study, and is considered a limitation. Therefore, this assumption simplifies the modelling without significantly affecting the accuracy of the results because the structural response is mainly governed by confinement and frictional interaction, and the effect of bond-slip on the overall behavior is relatively small. Since the rebars were present in the AS60S30 CFFT model, the embedded constraint was utilized to model the interaction between concrete and rebars. This approach allows the rebars to deform with the concrete, along with accurate stress transformation and kinematic compatibility. The meshing and boundary conditions of the CFST-2 and A60S30 CFFT model are shown in Figure 6.

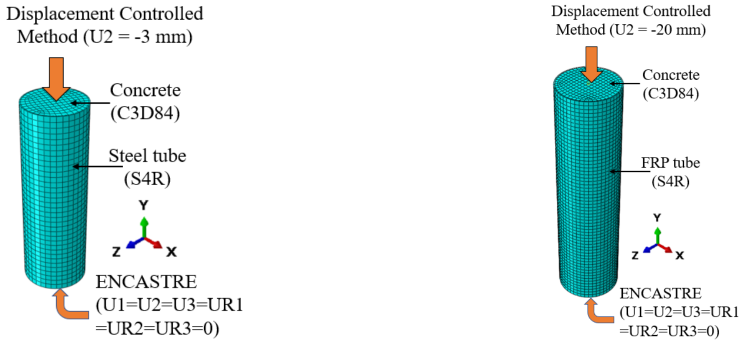

(a) CFST model (CFST-2) [25] (b) CFFT model (A60S30) [26]

Figure 6: Meshing and boundary conditions of the validated models

D. Validation of the proposed FEM model

The FEM analysis was performed using a static general analysis approach in Abaqus [22]. Since the mesh size directly affects the result in FEM analysis, the mesh-sensitive analysis was conducted in this study of different mesh sizes, including 10 mm, 15 mm, 20 mm, 25 mm, and 30 mm. Table 3 shows the comparison of test results between experimental and proposed FEM models for both CFST-2 [25] and A60S30 CFFT [26] model with different mesh sizes. Figure 7 shows the comparison of the load-displacement curve between the experimental and proposed FEM model for both the CFST-2 and A60S30 CFFT model, while Figure 8 shows the comparison of the failure modes.

Table 3: Comparison of test results between experimental and FEM model

Model	FEM Mesh Size (mm)	Experimental				Proposed FEM model				E in P_u (%)
		$\Delta_{y,exp}$ (mm)	$P_{y,exp}$ (kN)	$\Delta_{u,exp}$ (mm)	$P_{u,exp}$ (kN)	$\Delta_{y,FEM}$ (mm)	$P_{y,FEM}$ (kN)	$\Delta_{u,FEM}$ (mm)	$P_{u,FEM}$ (kN)	
CFST-2	10	0.63	625.5	1.14	717	0.6	628.7	1.05	723.1	0.85
	15					0.57	612.1	1.02	731.4	2.01
	20					0.56	600.9	1.03	716.8	0.13
	25					0.56	603.2	1.04	718.1	0.15
	30					0.58	590.6	1.02	704.5	1.74
A60S30 CFFT model	10	1.35	890	17.38	1652	1.15	824.3	16.99	1717.1	3.94
	15					1.14	820.2	16.97	1708.9	3.45
	20					1.14	810.5	16.98	1688.7	2.22
	25					1.13	802.4	17	1673.1	1.28
	30					1.13	801.8	17	1665	0.79

Note: $\Delta_{y,exp}$, $P_{y,exp}$, $\Delta_{u,exp}$, $P_{u,exp}$ represent yield displacement, yield load, peak displacement, and peak load, respectively obtained from an experiment; $\Delta_{y,FEM}$, $P_{y,FEM}$, $\Delta_{u,FEM}$, $P_{u,FEM}$ represent yield displacement, yield load, peak displacement, and peak load, respectively obtained from the proposed FEM model; E represents the error obtained in peak load between experimental and FEM model.

According to the results presented in figures and tables, the proposed FEM model with a mesh size of 25 mm showed better accuracy for both CFST-2 and A60S30 CFFT models, with an error in peak load of 0.15% and 1.28%, respectively. This close agreement is attributed to the use of validated constitutive models, appropriate boundary conditions, and the adoption of material parameters directly from well-established literature. For the CFST-2 model, the predicted failure mode is similar to the experimental test conducted by Wu et al. [25], indicating that it effectively captures the governing failure mechanism of the confined CFST column. In particular, the stress concentration is higher at the mid-height of the column, which is consistent with the experimentally observed behavior. This indicates that the central region of the column experienced maximum confinement and stress under uniform axial loading. The stress gradually decreased toward the ends, reflecting the influence of the boundary conditions. On the other hand, for the A60S30 CFFT column, the proposed FEM model showed localized fiber tensile damage in the FRP tube, which is also similar to the rupture pattern observed in the experimental model conducted by Mohamed et al. [26]. The damage distribution, evaluated using the HSNFCCRT parameter, indicates that rupture initiates at the top of the column, near the loading region, where stress concentration is highest. Therefore, the numerical model is capable of predicting the rupture behavior and failure mechanism of the FRP-confined column. Nevertheless, the minimal discrepancies in the failure modes and load-displacement curve are attributed to the differences in boundary conditions and loading conditions between the experimental and FEM model.

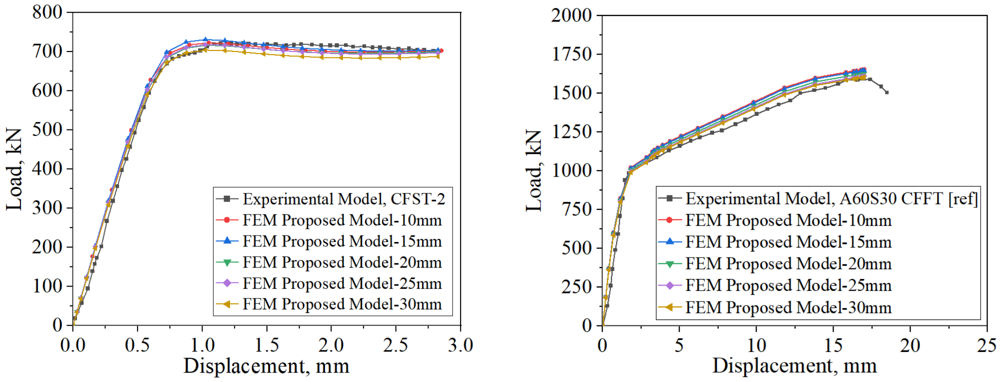

(a) CFST model (CFST-2) [25] (b) CFFT model (A60S30) [26]

Figure 7: Comparison of the load-displacement curve between the experimental and proposed FEM model

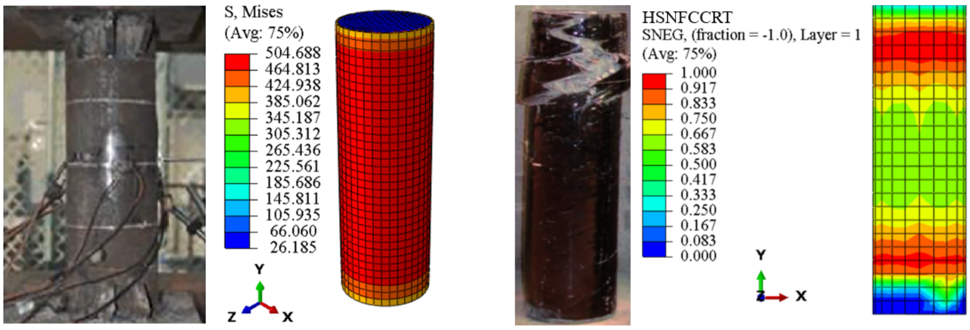

(a) CFST model (CFST-2) [25] (b) CFFT model (A60S30) [26]

Figure 8: Comparison of failure mode between experimental and proposed FEM model

E. Reference model for further study

Since a mesh size of 25 mm showed better results and improved convergence stability, it was adopted for the further analysis of both CFST and CFFT columns. Columns with similar height, diameter, and tube thickness were adopted to enable direct and unbiased comparison between their structural behavior and confinement effect. Furthermore, an unconfined concrete strength of 30 MPa was adopted for both CFST and CFFT columns, while the same rebar configuration as that utilized in the A60S30 CFFT column was applied to study the influence of rebars on their structural behavior. The reference model was named as CFST-T2-R10-SR4-Cir and CFFT-T2-R10-SR4-Cir for the CFST column and the CFFT column, respectively, where T2 suggests a tube thickness of 2 mm, R10 suggests a rebar diameter of 10 mm, SR4 suggests a slenderness ratio of 4, and Cir suggests circular shape. The detailed drawing of

CFST-T2-R10-SR4-Cir and CFFT-T2-R10-SR4-Cir is shown in Figure 9. Simultaneously, the material properties of rebars, steel tube, and FRP tube, loading method, boundary conditions, and the interaction modules were kept similar to the validated model. The comparison between these models with varying tube thickness, rebar ratio/diameter, slenderness ratio, and shape of the column is analyzed and explained in detail in the sections below.

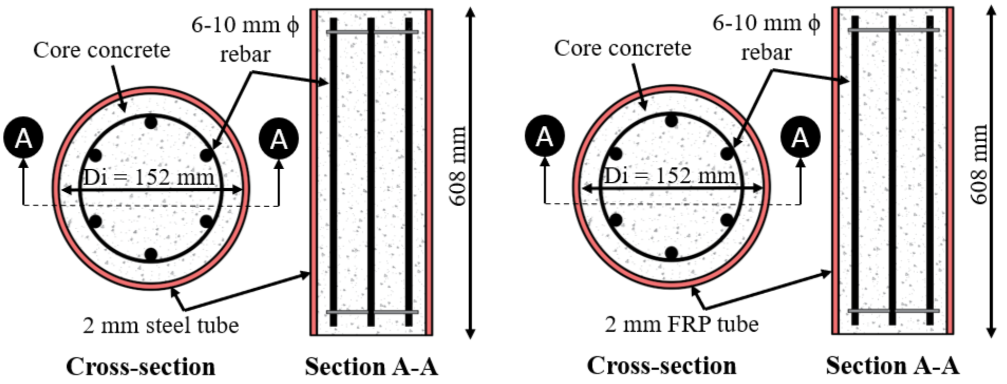

(a) CFST-T2-R10-SR4-Cir (b) CFFT-T2-R10-SR4-Cir

Figure 9: Detailed drawing of reference model

3. STRUCTURAL RESPONSE OF CFST AND CFFT COLUMNS UNDER PARAMETRIC VARIATIONS

A. Structural response of varying tube thickness in CFST and CFFT columns

A series of FEM analyses was conducted by varying the tube thickness to 2 mm, 4 mm, 6 mm, and 8 mm. All other geometrical and material properties were kept the same as those of reference models CFST-T2-R10-SR4-Cir and CFFT-T2-R10-SR4-Cir, with tube thickness being the only parameter varied. The initial yield stiffness (*K*i), post-yield stiffness (*K*p), and ductility index (μ) were calculated from the load-displacement curve obtained from the FEM analysis by utilizing Eq. (23), Eq. (24), and Eq. (25), respectively. The results for the structural response of the CFST and CFFT columns based on varying tube thickness are shown in Figure 10.

$$K_i = \frac{P_y}{\Delta_y} \tag{23}$$

$$K_p = \frac{P_u - P_y}{\Delta_u - \Delta_y} \tag{24}$$

$$\mu = \frac{\Delta_{ult}}{\Delta_{y}} \tag{25}$$

Where Δ_y, P_y, Δ_u, P_u, and Δ_{ult} represent yield displacement, yield load, peak displacement, peak load, and ultimate displacement corresponding to ultimate load (P_{ult} = 85% of peak load for descending branch of the curve), respectively.

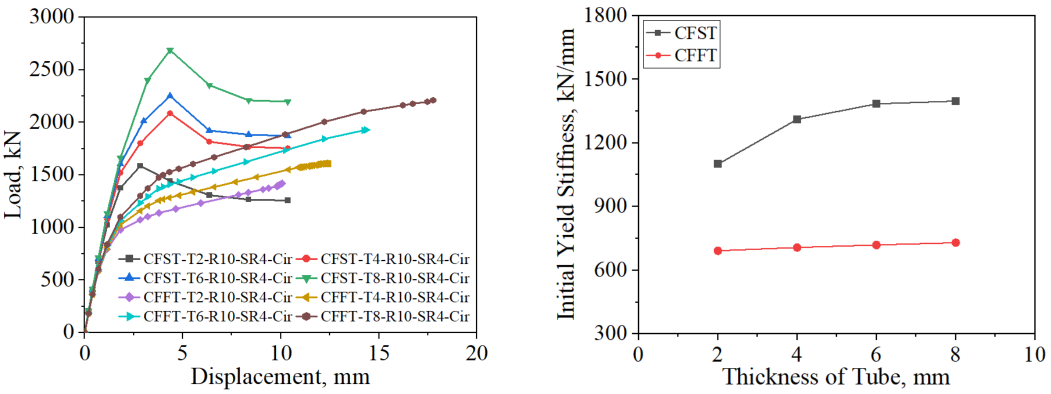

(a) Load-displacement curve (b) Initial stiffness

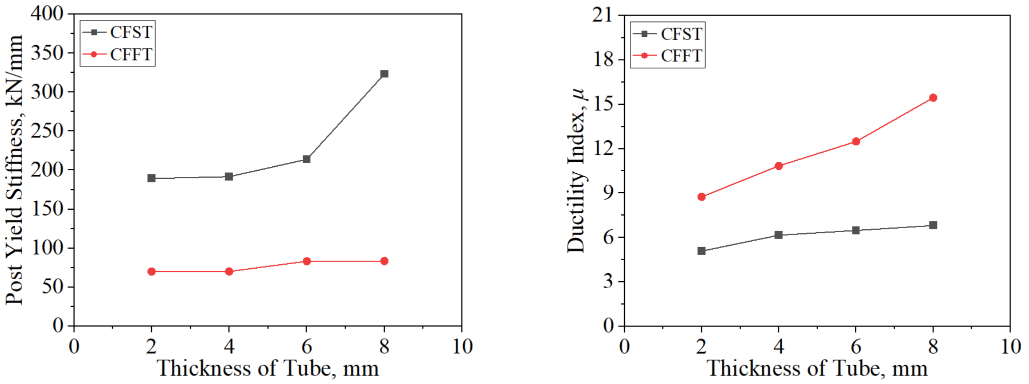

(c) Post-yield stiffness (d) Ductility index

Figure 10: Response of the CFST and CFFT columns based on varying tube thickness

According to the figure, when the tube thickness was increased from 2 mm to 8 mm, the load-bearing capacity increased significantly from 1584.93 kN to 2687.16 kN in the CFST column (corresponding to a 69.44% increase), while it increased from 1420.93 kN to 2210.93 kN in the CFFT column (corresponding to a 55.6% increase). For the CFST column, the initial stiffness, post-yield stiffness, and ductility index increased from 1100.28 kN/mm to 1397.67 kN/mm (i.e., 27.023% increase), 189.4 kN/mm to 323.41 kN/mm (i.e., 70.75% increase), and 5.09 to 6.82 (34% increase), respectively. Simultaneously, for the CFFT column, the initial stiffness, post-yield stiffness, and ductility index increased from 692.28 kN/mm to 730.17 kN/mm (i.e., 5.47% increase), 70.05 kN/mm to 82.5 kN/mm (i.e., 17.8% increase), and 8.76 to 15.45 (i.e., 76.37% increase), respectively. The CFST model showed higher stiffness compared to CFFT models because of the significantly higher modulus of elasticity of steel than the FRP materials. This allows the steel tube to resist the load and increase the axial stiffness of the column, while also providing confinement. Hence, stiffness increased significantly in CFST columns with an increase in steel tube thickness. However, in CFFT columns, the FRP mainly provides confinement with limited contribution to axial stiffness.

Overall, increasing tube thickness significantly enhances the structural behavior of both CFST and CFFT columns, but the influence varies between the two systems due to their different material characteristics and confinement mechanisms. While CFST columns exhibited higher stiffness and strength, CFFT columns indicated better ductility than the CFST columns, with an increase in tube thickness. This is attributed to the confinement mechanism of FRP, which allows greater lateral expansion of concrete before rupture, resulting in enhanced deformation capacity and energy-absorption potential.

B. Structural response of varying rebar size in CFST and CFFT columns

The varying rebar diameters of 0 mm (no reinforcement in column), 10 mm, 12 mm, and 16 mm were utilized in this study to study their effect on CFST and CFFT columns. All other properties of the column, such as shape, slenderness ratio, tube thickness, and concrete diameter, were kept similar to the CFST-T2-R10-SR4-Cir and CFFT-T2-R10-SR4-Cir reference models, while the rebar diameter was only varied. Figure 11 shows the response of the CFST and CFFT columns based on varying rebar diameter.

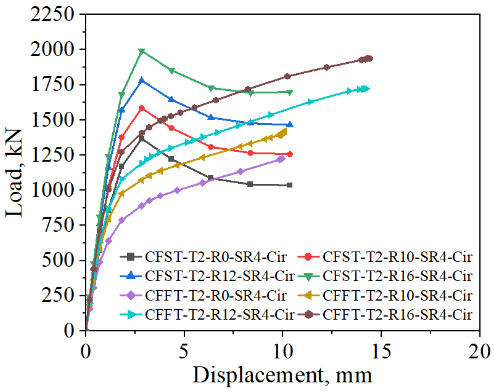

(a) Load-displacement curve

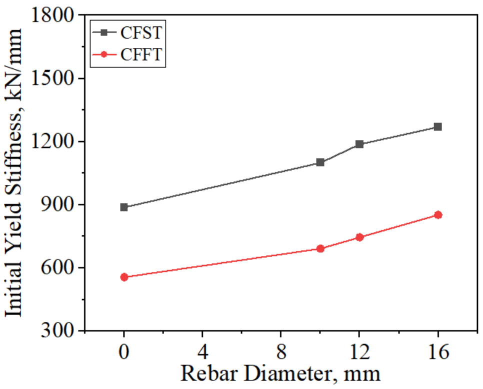

(b) Initial stiffness

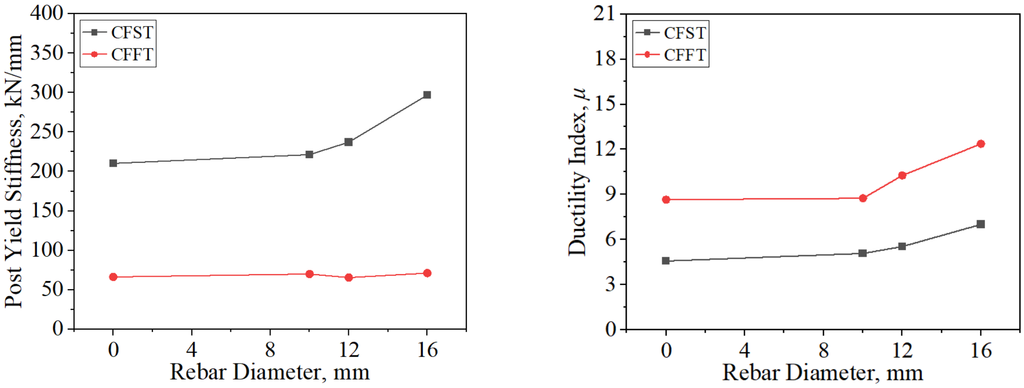

(c) Post-yield stiffness

(d) Ductility index

Figure 11: Response of the CFST and CFFT columns based on varying rebar diameter

The results suggest that when the rebar diameter was increased from 0 mm (no reinforcement) in CFST-T2-R0-SR4-Cir column to 16 mm in CFST-T2-R16-SR4-Cir column, the load bearing capacity, initial stiffness, and post-yield stiffness increased significantly from 1162.7 kN to 1692.8 kN (46% increase), 888.2 kN/mm to 1270.1 kN/mm (43% increase), 210.3 kN/mm to 296.9 kN/mm (41.2% increase), respectively. Similarly, in CFFT column, increasing rebar diameter from 0 mm to 16 mm increased the load-bearing capacity, and initial stiffness from 1224.4 kN to 1938.9 kN (58.4% increase), and 556.9 kN/mm to 852.52 kN/mm (53% increase), respectively, however the increase in post-yield stiffness was very minimal compared to CFST column, which is 7.3% increase. The ductility index enhanced with an increase in rebar diameter from 0 mm to 16 mm in both CFST and CFFT columns by 52.9% and 39.9%, respectively.

This behavior can be attributed to the interaction between longitudinal reinforcement and confinement. The longitudinal rebar delays the cracking of the concrete by contributing to resisting the load. In CFST columns, the steel tube provides strong and continuous confinement along with direct axial stiffness, resulting in a balanced increase in both strength and stiffness. In contrast, in CFFT columns, the lateral confinement provided by the FRP tube enhances the axial strength and strain capacity of the confined concrete. As the rebar diameter increases, higher lateral strains develop in the concrete core, which activates stronger confinement from the FRP. However, due ot low elastic modulus of FRP, its contribution to the axial stiffness remains limited. Hence, the improvement in post-yield stiffness remains relatively small compared to CFST columns.

Overall, longitudinal rebars are particularly effective in improving overall strength and energy dissipation capacity of the columns, with improved post-yield behavior in the CFST column than the CFFT column due to better confinement and axial stiffness provided by the steel tube than the FRP tube.

C. Structural response of varying slenderness ratio in CFST and CFFT columns

The varying geometric slenderness ratios (ratios of length of column to diameter of column or L/D) of 2, 4, 6, and 8 were utilized in this study to study their effect on the structural behavior of the CFST and CFFT columns. Figure 12 shows the response of the CFST and CFFT columns based on varying slenderness ratios.

According to the results and curve, the load-bearing capacity, initial stiffness, and post-yield stiffness decrease for both the CFST and CFFT columns with an increase in slenderness ratio. For the CFST column, when the slenderness was increased from 2 to 4, the load bearing capacity, initial stiffness, and post-yield stiffness decreased by 11.37%, 70.8%, and 28.07%, respectively. Simultaneously, for the CFFT column, these values decreased by 16.4%, 71.6%, and 46.5%, respectively. However, the ductility index increased for both CFST and CFFT columns with an increase in slenderness ratio from 2 to 4 by 62.4% and 72.3%, respectively. This overall behavior indicates that the columns become prone to buckling with an increase in slenderness ratio (L/D), and buckling effects become prominent for L/D ≥ 6. Columns with L/D < 4 primarily exhibit strength and stability-controlled response, due to their higher global flexural stiffness, which limits lateral deflection. As the slenderness ratio increases, the flexural stiffness of the column decreases, making it more sensitive to second-order (P-Δ) effects, affecting the stability, lateral displacement, and strength of the column. However, slender columns (L/D ≥ 6) undergo large deformation before reaching failure, even though their load-bearing capacity is lower.

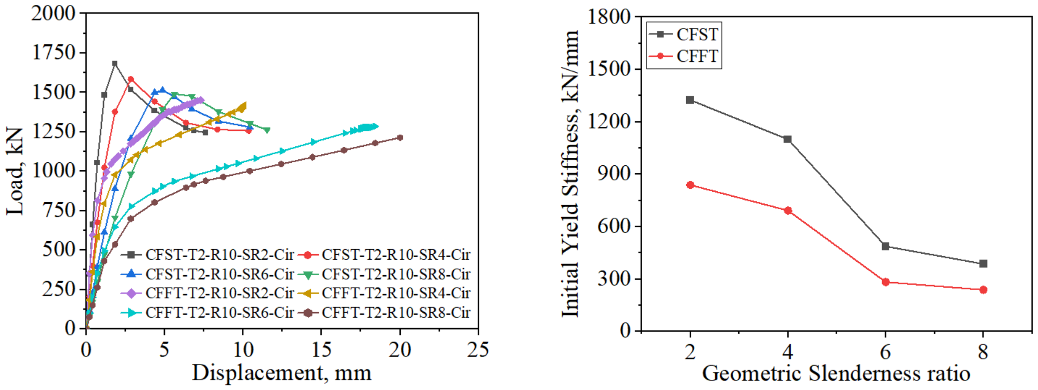

(a) Load-displacement curve

(b) Initial stiffness

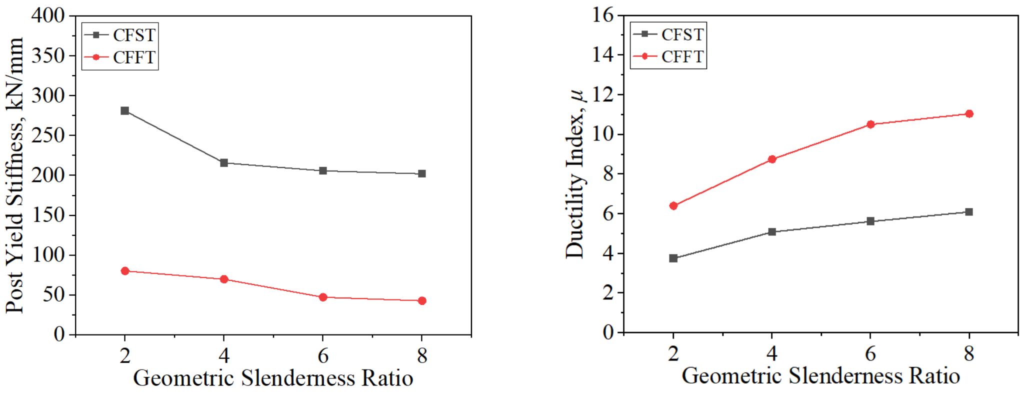

(c) Post-yield stiffness (d) Ductility index

Figure 12: Response of the CFST and CFFT columns based on varying slenderness ratio

D. Structural response of varying shapes of CFST and CFFT columns

The varying shapes of CFST and CFFT columns, such as circle, square, rectangle, and hexagon, were utilized in this study to study their effect on the structural performance. For the circular column, the reference models CFST-T2-R10-SR4-Cir and CFFT-T2-R10-SR4-Cir were modeled with a overall diameter of 156 mm and height of 608 mm. The square columns were modeled with a cross-section of 156*156 mm, the rectangular columns were modeled with a cross-section of 122*200 mm, and the hexagon columns were modeled with a circumscribed diameter of 156 mm. All other material properties and geometric properties, including slenderness ratio, thickness of tube, and reinforcement ratio, were kept similar to the reference models. Figure 13 shows the response of the CFST and CFFT columns based on the varying shapes.

From the figure, it can be seen that, in the CFST column, the load-bearing capacity of the square, rectangular, and hexagonal columns was reduced by 16.39%, 31.9%, and 10.43%, respectively, compared to the circular CFST column (CFST-T2-R10-SR4-Cir), suggesting a strong dependence on the cross-sectional area or shape of the column. Also, it was observed that the circular CFST column (CFST-T2-R10-SR4-Cir) showed the highest initial stiffness among various shape columns, which was 15.7%, 22.1%, and 6.9% greater than the square, rectangular, and hexagonal shape CFST columns, respectively. However, the square shape column (CFST-T2-R10-SR4-Sqr) showed the highest post-yield stiffness among various columns, which was 49.2%, 31.7%, and 137.4% greater compared to circular, rectangular, and hexagonal shape columns, respectively. The ductility index was also higher in the circular column (CFST-T2-R10-SR4-Cir), which was enhanced by 37.2%, 56%, and 3.85%, respectively, compared to square, rectangular, and hexagonal shape columns, respectively.

Similar to the CFST column, the CFFT column also showed higher peak strength in circular column (CFFT-T2-R10-SR4-Cir), which increased by 12.1%, 25.1%, and 7.2% compared to square, rectangular, and hexagonal shape columns, respectively. The initial stiffness, post-yield stiffness, and ductility index were also higher in the circular column among various shape CFFT columns. In comparison with the square, rectangular, and hexagonal columns, the ductility index in the circular column (CFFT-T2-R10-SR4-Cir) increased by 13.1%, 13.92%, and 3.1%, respectively.

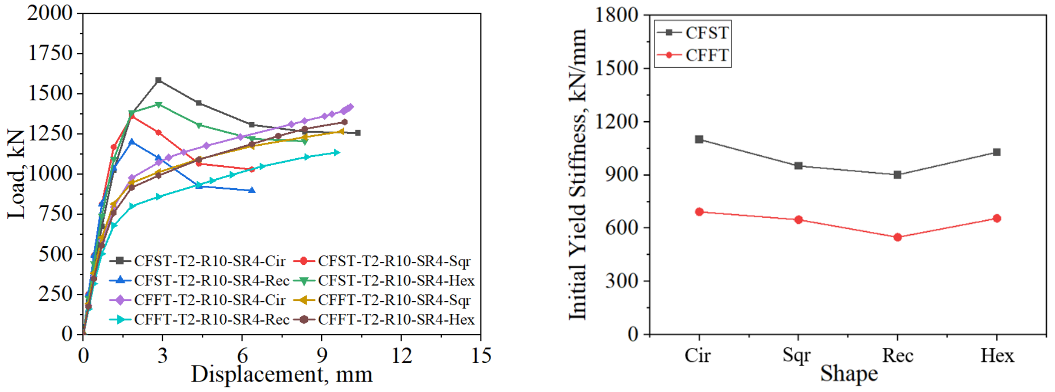

(a) Load-displacement curve (b) Initial stiffness

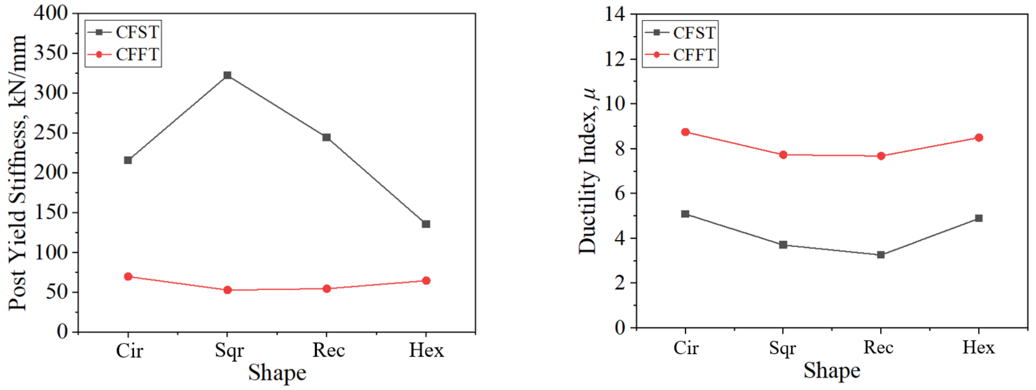

(c) Post-yield stiffness (d) Ductility index

Figure 13: Response of the CFST and CFFT columns based on varying shape

This overall behavior indicates that the circular section provides the most balanced performance in terms of stiffness, strength, and ductility, due to better and uniform radial confinement effect provided by the steel or FRP tube. This uniform confinement delays the buckling and failure mechanism of the column, allowing it to resist load more effectively. However, in other models, including square, rectangle, and hexagon sections, the confinement provided by the steel or FRP tube is non-uniform due to sharp corners. These non-uniform confinement effects cause stress concentrations in the corner areas, leading to localized weakness and making the column more susceptible to premature failure of concrete.

4. CONCLUSION

This paper presents a comparative analysis of CFST and CFFT columns under axial loading using finite element method. The finite element modeling was validated using a literature review for both CFST and CFFT column, separately. Furthermore, a parametric study was conducted on the tube thickness, reinforcement ratio, cross-sectional shape, and slenderness ratio for both CFST and CFFT columns, which provides valuable insights into the performance differences, particularly in terms of load-bearing capacity, stiffness, and ductility. The developed FEM model demonstrated a strong agreement with experimental results from the literature, hence these models can be utilized further to expand the scope of research and design optimization for the CFST and CFFT columns. The conclusions drawn from the research are presented below:

1. In CFST column, when the cross-sectional shape was changed from circular to square, rectangular, and hexagonal, the load-bearing capacity decreased by 16.39%, 31.9%, and 10.43%, respectively. And in CFFT column, the load-bearing capacity of cicular column is greater than square, rectangular, and hexogonal column by 12.1%, 25.1%, and 7.2%, respectively. This indicates that the circular column provides uniform confinement due to lack of its sharp edges, which ensures better load distribution and minimizes stress concentrations at corners.
2. Increasing the tube thickness from 2 mm to 8 mm enhanced the peak strength, initial stiffness, and post-yield stiffness of CFST column by 69.44%, 27.02%, and 70.75%, respectively. However, for the CFFT column, the peak strength increased by 55.6%, with minimal changes observed in the initial stiffness and post-yield stiffness. This behavior is attributed to the contribution of the steel tube in the CFST column, which improve stiffness and strength due to its higher modulus of elasticity compared to the FRP tube.
3. When the L/D ratio was increased from 2 to 4 mm, the load-bearing capacity, initial-stiffness, and post-yield stiffness in CFST column decreased by 11.37%, 70.8%, and 28.07%, respectively, whereas in CFFT column, these values diminished by 16.4%, 71.6%, and 46.5%, respectively. In contrast, the ductility index in both CFST and CFFT columns, enhanced by 62.4%, and 72.3%, respectively. This behavior shows that with an increase in L/D ratio, column becomes prone to buckling, with L/D ≥ 6 showing significant buckling effects and larger deformation before failure, despite reduced load-bearing capacity.
4. Compared to the CFST column without rebar, the column with a 16 mm ϕ rebar demonstrated significant improvement in load-bearing capacity, initial stiffness, post-yield stiffness, and ductility index, increasing by 46%, 43%, 41.2%, and 52.9%, respectively. In the CFFT column, peak strength, initial-stiffness, and ductility index increased by 58.4%, 53%, and 39.9%, while post-yield stiffness decreased slightly by 7.3%. This suggests that longitudinal rebars in CFST columns provide strong confinement and axial stiffness, while in CFFT columns, higher lateral strains develop in the concrete core with an increase in rebar diameter, however, due to low elastic

modulus of FRP tube, its contribution remains limited.

All the findings in this paper are solely dependent on numerical analysis, and no experimental test was carried out, which is a limitation of this study. In addition, the FEM model in this study neglects bond-slip behavior due to lack of detailed interface properties, and simplifies interaction modules with a friction coefficient, which may affect the accuracy of the results. Furthermore, the constitutive models used are based on specific experimental conditions, limiting their applicability outside the calibrated range of material properties and confinement levels. In the future, experimental tests should be carried out to validate the FEM models of CFST and CFFT columns. Based on these results, an analytical model should be generated to establish a reliable design recommendation and promote the safe implementation of these columns in Nepal or elsewhere. Moreover, durability, creep, shrinkage, and cyclic tests should be conducted to determine the behavior of CFST and CFFT columns under harsh environmental conditions, and in seismic regions.

ACKNOWLEDGEMENT

This research received no external funding and was conducted solely for academic purposes, with the aim of contributing to the advancement of the structural field in Nepal.

REFERENCES

[1] F. Huang, X. Yu, and B. Chen, “The structural performance of axially loaded CFST columns under various loading conditions,” Steel Compos. Struct., vol. 13, no. 5, pp. 451–471, 2012. https://doi.org/10.12989/scs.2012.13.5.451

[2] K. Shrestha, B. Jaishi, A. Paudel, B. Chen, and J. Liu, “First CFST Arch Bridge in Nepal,” in Proceedings of ARCH 2023, vol. 32, B. Briseghella, A. Contento, and J. Liu, Eds., in Structural Integrity, vol. 32. , Cham: Springer Nature Switzerland, 2025, pp. 191–200. https://doi.org/10.1007/978-3-031-83508-7_21.

[3] Q. S. Khan, M. N. Sheikh, and M. N. Hadi, “Axial compressive behaviour of circular CFFT: Experimental database and design-oriented model,” Steel Compos. Struct., vol. 21, no. 4, pp. 921–947, 2016. http://conference.ioe.edu.np/publications/ioegc14/IOEGC-14-104-F3-5-588.pdf

[4] Y. Diao, S. He, Y. Zou, and Z. Yan, “Axial compression performance of circular and square CFST stub columns with varying glass aggregates replacement ratio and reinforcement forms,” Constr. Build. Mater., vol. 492, p. 142838, 2025. https://doi.org/10.1016/j.conbuildmat.2025.142838

[5] C. Song, Y.-B. Wang, G.-Q. Li, and J. R. Liew, “Influence of slenderness on confining effect of axially loaded circular CFST columns with high-strength materials,” Eng. Struct., vol. 333, p. 120041, 2025. https://doi.org/10.1016/j.engstruct.2025.120041

[6] J.-K. Zhou, W.-K. Lin, S.-X. Guo, J.-J. Zeng, and Y.-L. Bai, “Behavior of FRP-confined FRP spiral reinforced concrete square columns (FCFRCs) under axial compression,” J. Build.

Eng., vol. 45, p. 103452, 2022. https://doi.org/10.1016/j.jobe.2021.103452

[7] M. Yang, D. Yu, Q. Qiu, and Y. Yu, “Finite element analysis and bearing capacity calculation of cross-shaped CFST columns under compressive load,” Heliyon, vol. 10, no. 7, 2024.

[8] Y. Zheng and S. Zeng, “Design of L-shaped and T-shaped concrete-filled steel tubular stub columns under axial compression,” Eng. Struct., vol. 207, p. 110262, 2020. https://doi.org/10.1016/j.engstruct.2020.110262

[9] A. Sadat Hosseini and P. Sadeghian, “Finite Element Modeling of Fiber-Reinforced Polymer Composite Tubes Filled with Concrete,” in Proceedings of the Canadian Society of Civil Engineering Annual Conference 2022, vol. 359, pp. 107–117, 2022. https://doi.org/10.1007/978-3-031-34027-7_8

[10] H. D. Phan, “Numerical analysis of seismic behavior of square concrete filled steel tubular columns,” J. Sci. Technol. Civ. Eng. JSTCE-HUCE, vol. 15, no. 2, pp. 127–140, 2021. https://doi.org/10.31814/stce.nuce2021-15(2)-11

[11] W. Li, X. Zhao, and Y. Lu, “Mechanism-based unified design formula for axially loaded CFST columns with various profiles,” J. Constr. Steel Res., vol. 211, p. 108163, 2023. https://doi.org/10.1016/j.jcsr.2023.108163

[12] B. R. Alnemrawi and R. Al-Rousan, “The detailed axial compression behavior of CFST columns infilled by lightweight concrete,” Buildings, vol. 14, no. 9, p. 2844, 2024. https://doi.org/10.3390/buildings14092844

[13] M. Hassam, L. Guo, and H. Li, “Compression performance of cross-shaped CFST columns under concentric and eccentric loading,” in Structures, Elsevier, 2025, p. 110828. https://doi.org/10.1016/j.istruc.2025.110828

[14] D. Huang, Z. Liu, Y. Lu, W. Ma, and S. Li, “Experimental and numerical investigation of bias performance of steel fiber-reinforced GRC-CFFT columns,” Eng. Struct., vol. 319, p. 118897, 2024. https://doi.org/10.1016/j.engstruct.2024.118897

[15] Q. S. Khan, M. N. Sheikh, and M. N. Hadi, “Experimental results of circular FRP tube confined concrete (CFFT) and comparison with analytical models,” J. Build. Eng., vol. 29, p. 101157, 2020. https://doi.org/10.1016/j.jobe.2019.101157

[16] L. Lam and J. G. Teng, “Design-oriented stress–strain model for FRP-confined concrete,” Constr. Build. Mater., vol. 17, no. 6–7, pp. 471–489, 2003. https://doi.org/10.1016/S0950-0618(03)00045-X

[17] M. Hussein Abdallah, M. Shazly, H. M. Mohamed, R. Masmoudi, and A. Mousa, “Nonlinear finite element analysis of short and long reinforced concrete columns confined with GFRP tubes,” J. Reinf. Plast. Compos., vol. 36, no. 13, pp. 972–987, Jul. 2017, http://doi.org/10.1177/0731684417698758

[18] A. Raza, A. ur Rehman, B. Masood, and I. Hussain, “Finite element modelling and theoretical predictions of FRP-reinforced concrete columns confined with various

FRP-tubes," in Structures, Elsevier, 2020, pp. 626–638. https://doi.org/10.1016/j.istruc.2020.04.033

[19] H. S. Mohamed et al., "Compressive behavior of elliptical concrete-filled steel tubular short columns using numerical investigation and machine learning techniques," Sci. Rep., vol. 14, no. 1, p. 27007, 2024. https://doi.org/10.1038/s41598-024-77396-5

[20] P. Xie, G. Lin, J. G. Teng, and T. Jiang, "Modelling of concrete-filled filament-wound FRP confining tubes considering nonlinear biaxial tube behavior," Eng. Struct., vol. 218, p. 110762, 2020. https://doi.org/10.1016/j.engstruct.2020.110762

[21] S. Song, D.-H. Son, B.-I. Bae, M.-S. Lee, and C.-S. Choi, "Finite element analysis for axial compressive behavior of CFT columns assembled with rectangular wave-shaped ribs," in Structures, Elsevier, 2024, p. 107324. https://doi.org/10.1016/j.istruc.2024.107324

[22] Dassault Systemes. ABAQUS documentation. Providence, RI, USA: Dassault Systemes; 2018.

[23] Z.-M. Yang, J. Chen, and M. Pandey, "Compressive behavior and design calculations of CFST slender columns with latticed annular steel part," J. Constr. Steel Res., vol. 223, p. 109028, 2024. https://doi.org/10.1016/j.jcsr.2024.109028

[24] R. Abdulkhudhur, M. Elwi, and H. Al-Quraishi, "Axial Compression Behavior of Concrete-Encased CFST Columns," Civ. Eng. J., vol. 11, no. 6, pp. 2255–2266, 2025. http://dx.doi.org/10.28991/CEJ-2025-011-06-05

[25] Q. Wu, Z. She, and H. Yuan, "Experimental study of UHPC-encased CFST stub columns under axial compression," in Structures, Elsevier, 2021, pp. 433–447. https://doi.org/10.1016/j.istruc.2021.03.053

[26] H. M. Mohamed and R. Masmoudi, "Axial Load Capacity of Concrete-Filled FRP Tube Columns: Experimental versus Theoretical Predictions," J. Compos. Constr., vol. 14, no. 2, pp. 231–243, 2010. http://doi.org/10.1061/(ASCE)CC.1943-5614.0000066

[27] L.-H. Han, X.-L. Zhao, and Z. Tao, "Tests and mechanics model for concrete-filled SHS stub columns, columns and beam-columns," Steel Compos. Struct. Int. J., vol. 1, no. 1, pp. 51–74, 2001. https://doi.org/10.12989/scs.2001.1.1.051

[28] L.-H. Han, G.-H. Yao, and X.-L. Zhao, "Tests and calculations for hollow structural steel (HSS) stub columns filled with self-consolidating concrete (SCC)," J. Constr. Steel Res., vol. 61, no. 9, pp. 1241–1269, 2005. https://doi.org/10.1016/j.jcsr.2005.01.004

[29] L.-H. Han, G.-H. Yao, and Z. Tao, "Performance of concrete-filled thin-walled steel tubes under pure torsion," Thin-Walled Struct., vol. 45, no. 1, pp. 24–36, 2007. https://doi.org/10.1016/j.tws.2007.01.008

[30] D. J. Carreira and K.-H. Chu, "Stress-strain relationship for plain concrete in compression," in Journal proceedings, pp. 797–804, 1985. https://doi.org/10.14359/10390

[31] J. Mazars and S. Grange, "Damage Model Strategies to Forecast Concrete Structure Behaviors Under Static and Dynamic Loadings," in Handbook of Damage Mechanics, G. Z.

Voyiadjis, Ed., Cham: Springer International Publishing, 2022, pp. 489–516. https://doi.org/10.1007/978-3-030-60242-0_77

[32] ACI Committee, 318. "Building code requirements for structural concrete (ACI 318-08) and commentary." American Concrete Institute, 2008.

[33] E. Hognestad, “Study of combined bending and axial load in reinforced concrete members,” Univ. Ill. Eng. Exp. Stn. Bull. No 399, 1951. https://www.ideals.illinois.edu/items/4902/bitstreams/19186/data.pdf

[34] Z. Tao, Z.-B. Wang, and Q. Yu, “Finite element modelling of concrete-filled steel stub columns under axial compression,” J. Constr. Steel Res., vol. 89, pp. 121–131, 2013. https://doi.org/10.1016/j.jcsr.2013.07.001

[35] V. K. Papanikolaou and A. J. Kappos, “Confinement-sensitive plasticity constitutive model for concrete in triaxial compression,” Int. J. Solids Struct., vol. 44, no. 21, pp. 7021–7048, 2007. https://doi.org/10.1016/j.ijsolstr.2007.03.022

[36] T. Yu, J. G. Teng, Y. L. Wong, and S. L. Dong, “Finite element modeling of confined concrete-II: Plastic-damage model,” Eng. Struct., vol. 32, no. 3, pp. 680–691, 2010. https://doi.org/10.1016/j.engstruct.2009.11.013

[37] F. E. Richart, A. Brandtzaeg, and R. L. Brown, “A study of the failure of concrete under combined compressive stresses,” Univ. Ill. Eng. Exp. Stn. Bull. No 185, 1928. https://www.ideals.illinois.edu/items/5277/bitstreams/20686/data.pdf

[38] G. Lin and J. G. Teng, “Three-Dimensional Finite-Element Analysis of FRP-Confined Circular Concrete Columns under Eccentric Loading,” J. Compos. Constr., vol. 21, no. 4, p. 04017003, 2017. https://doi.org/10.1061/(ASCE)CC.1943-5614.0000772

[39] Européen, C. "Eurocode 2: Design of concrete structures—Part 1-1: General rules and rules for buildings." London: British Standard Institution 37, 2004.

[40] M. Samaan, A. Mirmiran, and M. Shahawy, “Model of Concrete Confined by Fiber Composites,” J. Struct. Eng., vol. 124, no. 9, pp. 1025–1031, 1998. https://doi.org/10.1061/(ASCE)0733-9445(1998)124:9(1025)

[41] F. Wang, B. Young, and L. Gardner, “Testing, numerical analysis and design of CFDST cross-sections with square stainless steel outer tubes in bending,” J. Constr. Steel Res., vol. 211, p. 108125, 2023. https://doi.org/10.1016/j.jcsr.2023.108125

[42] E. Burak and A. Tuncan, “Determination of frictional behavior between concrete and steel tube interaction,” in Proceedings of the 7th European Conference on Steel and Composite Structures Eurosteel, pp. 521–522, 2014.